

Sylvain Terraz
Alexandru Cernicanu
Matthieu Lepetit-Coiffé
Magalie Viallon
Rares Salomir
Gilles Mentha
Christoph D. Becker

Radiofrequency ablation of small liver malignancies under magnetic resonance guidance: progress in targeting and preliminary observations with temperature monitoring

Received: 25 March 2009
Revised: 6 July 2009
Accepted: 6 August 2009
Published online: 16 September 2009
© European Society of Radiology 2009

S. Terraz (✉) · A. Cernicanu ·
M. Lepetit-Coiffé · M. Viallon ·
R. Salomir · C. D. Becker
Department of Radiology,
University Hospitals of Geneva,
Rue Gabrielle-Perret-Gentil 4,
1211 Geneva 14, Switzerland
e-mail: sylvain.terraz@hcuge.ch
Tel.: +41-22-3727094
Fax: +41-22-3727072

G. Mentha
Department of Visceral Surgery
and Transplantation,
University Hospitals of Geneva,
Geneva, Switzerland

Abstract *Objectives:* To evaluate the feasibility and effectiveness of magnetic resonance (MR)-guided radiofrequency (RF) ablation for small liver tumours with poor conspicuity on both contrast-enhanced ultrasonography (US) and computed tomography (CT), using fast navigation and temperature monitoring. *Methods:* Sixteen malignant liver nodules (long-axis diameter, 0.6–2.4 cm) were treated with multipolar RF ablation on a 1.5-T wide-bore MR system in ten patients. Targeting was performed interactively, using a fast steady-state free precession sequence. Real-time MR-based temperature mapping was performed, using gradient echo–echo planar imaging (GRE-EPI) and hardware filtering. MR-specific treatment data were recorded. The mean follow-up time was 19 ± 7 months. *Results:* Correct placement of RF electrodes was

obtained in all procedures (image update, <500 ms; mean targeting time, 21 ± 11 min). MR thermometry was available for 14 of 16 nodules (88%) with an accuracy of 1.6°C in a non-heated region. No correlation was found between the size of the lethal thermal dose and the ablation zone at follow-up imaging. The primary and secondary effectiveness rates were 100% and 91%, respectively. *Conclusions:* RF ablation of small liver tumours can be planned, targeted, monitored and controlled with MR imaging within acceptable procedure times. Temperature mapping is technically feasible, but the clinical benefit remains to be proven.

Keywords Radiofrequency ablation · Magnetic resonance fluoroscopy · Magnetic resonance thermometry · Hepatocellular carcinoma · Liver metastases

Introduction

Image-guided radiofrequency (RF) ablation is gaining increasing acceptance as a local treatment of malignant hepatic lesions in well-defined clinical settings [1–4]. Ultrasonography (US) and computed tomography (CT) are currently the preferred imaging methods for guidance of RF ablation, as they are readily available, quick, precise and accessible at acceptable cost. However, magnetic resonance (MR) imaging with specific contrast materials is currently the most sensitive method for detecting liver tumours [5–7] and some small neoplastic nodules are only visible with this imaging modality. Therefore, it is desirable in some instances

to be able to perform RF ablation under MR guidance. In addition, MR imaging at high field (1 T and above) is also the only technique that offers the potential to map temperature and energy deposition of tissue during the ablation procedure, thus enabling the operator to monitor the progress and define the endpoint of energy deposition [8–10].

Although RF ablation is the preferred technique for local treatment of liver tumours of limited size, the number of clinical reports in the literature on MR-guided RF ablation is still limited. Some preliminary studies have demonstrated that MR-based targeting is lengthy, requiring dedicated hardware and software and long periods of protected time in the MR suite [11–14]. Nonetheless, these studies have

demonstrated the feasibility of targeting either with low-field open or closed-bore MR systems. Most interventionists currently rely on empirical parameters for energy deposition, rather than direct monitoring of tissue changes induced by RF energy. The clinical experience of real-time monitoring by MR thermometry is now very limited, due to technical difficulties, such as RF generator interference with MR image acquisition [15].

Image-guided tumour ablation has been defined in distinct steps, namely planning, targeting, monitoring, controlling and follow-up [16]. The purpose of this study was to evaluate whether all these steps, including RF electrode targeting under high temporal resolution navigation and monitoring of temperature and energy deposition during RF application, can be performed effectively in small liver tumours that are detectable only with MR imaging.

Materials and methods

Patients and lesions

From November 2006 to October 2008, a total of 98 malignant hepatic tumours in 61 patients not suitable for surgical resection were treated with image-guided RF ablation in our institution. Following multidisciplinary discussion and informed consent, 53 treatment sessions (66%) were performed under US guidance, 15 sessions (19%) under CT guidance, and 12 sessions (15%) under MR guidance. The MR-guided procedures form the basis of this prospective study, which was approved by the institutional ethics review board.

Sixteen malignant hepatic nodules in 10 patients (six men, four women; age, 63 ± 7 years; range, 54–79) were readily visible on T1- or T2-weighted MR images, but either invisible or not sufficiently conspicuous with contrast-enhanced US and CT (Table 1). Three patients had hepatocellular carcinoma (HCC) in cirrhosis, diagnosed according to international guidelines with imaging ($n=2$) or MR-guided biopsy ($n=1$) [17]. Six patients with known colorectal cancer had liver metastases, diagnosed with imaging ($n=5$) or MR-guided biopsy ($n=1$). One patient had local progressive disease in the periphery of a single liver metastasis from squamous cell carcinoma of the right upper pulmonary lobe. The mean long-axis diameter of the nodules was 1.5 ± 0.5 cm (0.6–2.4). Seven nodules were located within 5 mm from vessels larger than 3 mm, whereas three nodules were located within 5 mm from the liver capsule.

MR-compatible RF ablation system

RF ablation was performed with a 470-kHz multipolar RF generator (Celon AG, Teltow, Germany) coupled with one or two internally cooled MR-compatible electrodes (active

tip length, 3 cm; shaft length, 15 cm) [18, 19]. The algorithm of energy deposition was based on the manufacturer's guidelines for power settings and included the resistance-controlled automatic power (RCAP) mode.

External hardware filtering of the transmission line was implemented between the RF generator and the electrodes, in order to reduce interference between generator harmonics and MR image acquisition frequency (Fig. 1). Stop-band RLC filters, tuned to 63.5 MHz and associated with ferrite cores, were placed inside the Faraday cage. The manufacturer approved these modifications and preliminary testing on gel phantoms and in vivo in pigs enabled us to perform simultaneous RF application and MR imaging safely and with acceptable image quality.

Radiofrequency ablation procedures

A radiologist experienced in hepatobiliary interventions and RF ablation for 8 years performed the twelve RF treatment sessions under general anaesthesia with an MR-compatible anaesthesia machine and monitoring devices. A prophylactic dose of 2 g of ceftriaxone was intravenously administered 1 h before the procedure and was repeated twice over 48 h. Diagnostic imaging and RF ablation procedures were performed on a 1.5-T interventional MR system (Espree; Siemens, Erlangen, Germany) with a closed bore (inner diameter, 70 cm; length, 120 cm) [12]. Patients were placed feet first on the MR table in either supine or left lateral decubitus position. The MR signal was received by six elements of a spine matrix coil and a 19-cm-diameter loop surface coil. A breathing sensor was placed around the chest wall for respiratory gating.

Planning

The RF electrode trajectory was planned from the entry point to the target tumour, avoiding critical structures, by using multiplanar reconstructions (MPR) of the 3D acquisition. Two orthogonal and oblique planes including the trajectory line were selected and transferred to the graphical slice-positioning (GSP) software of an in-room user interface (Interactive Frontend; Siemens, Erlangen, Germany). The entry point was determined by moving the little finger at the skin surface.

The pre-procedural imaging protocol included a T2-weighted half-Fourier acquisition single-shot turbo spin-echo (HASTE) sequence (repetition time (TR), 1,000 ms; echo time (TE), 83 ms; slice thickness, 4 mm) and a T2-weighted segmented turbo spin-echo (TSE) sequence with fat saturation (TR, 6,000 ms; TE, 104 ms; slice thickness, 6 mm), obtained in the transverse plane with navigator triggering. A high-resolution isotropic T1-weighted volume-interpolated breath-hold examination (VIBE) sequence with fat saturation (TR, 5.6 ms; TE, 2.7 ms; slice thickness, 2 mm)

Table 1 Characteristics of the patients and their malignant hepatic nodules

Patient	Prior treatment	Lesion number	Tumour histology	Long-axis diameter (cm)	Short-axis diameter (cm)	Vessel vicinity
A	TACE	1	HCC	2.4	2.0	PV
B	Resection	2	CRM	2.1	1.5	–
		3	CRM	1.6	1.1	HV
		4	CRM	1.8	1.2	–
C	Resection	5	CRM	1.8	1.0	HV
		6 ^a	CRM	1.4	0.9	HV
D	Resection	7	CRM	1.3	1.2	IVC
		8	CRM	1.3	0.7	–
E	Resection	9	CRM	1.8	1.1	–
F	RFA	10	LUM	1.8	1.3	–
		11	LUM	1.7	1.2	HV
G	–	12 ^b	CRM	0.8	0.6	–
H	TACE	13	HCC	1.4	1.0	PV
I	–	14	HCC	1.6	1.3	–
J	–	15 ^c	CRM	0.9	0.7	–
		16 ^c	CRM	0.6	0.5	–

The diameter of the nodules was 1.5 ± 0.5 cm (0.6–2.4 cm) in the long-axis and 1.1 ± 0.4 cm (0.5–2.0 cm) in the short-axis, with corresponding volumes of 1.2 ± 1.2 cm³ (0.1–5.0 cm³)

RFA radiofrequency ablation (under US guidance), TACE transarterial chemoembolisation, CRM metastasis from colorectal carcinoma, HCC hepatocellular carcinoma, LUM metastasis from squamous cell carcinoma of the lung, HV hepatic vein, IVC inferior vena cava, PV portal vein

^aRetreatment of the local tumour progression of lesion 5

^bMetachronous metastasis in the left lobe prior to extended right hepatectomy

^cMetachronous metastases in the right lobe prior to extended left hepatectomy

was acquired in the transverse orientation. If the lesion was not sufficiently visible on the T1-weighted VIBE sequence, it was repeated 20 min after a slow infusion of 0.5 µmol/kg of body weight of mangafodipir (Teslascan; GE Healthcare, Oslo, Norway).

Targeting

The patient was draped in a sterile fashion including the surface coil. The interventional radiologist incised the skin at the entry point, moved the RF electrode forward and followed its progression in almost real time on the MR-compatible monitor of the user interface placed next to the magnet bore. “Fluoroscopic” MR images were obtained on both axial and sagittal oblique perpendicular planes, which were interactively readjusted to the actual location of the RF electrode by a physicist inside the MR-suite controlling the GSP software with an MR-compatible mouse.

The interventional sequence was a dedicated, balanced steady-state free precession (bSSFP) interleaved radial sequence that was specially designed for the purpose of MR-guided interventions (IRTTT; Siemens, Erlangen, Germany) and consisted of the following image parameters: radial views, 64; sliding window width, 5; TR, 4.3 ms; TE, 2.2 ms; flip angle (FA), 70°; bandwidth (BW) 558 Hz/pixel;

matrix, 128×128; voxel size, 3×3×5 mm³; update rate, 275 ms. The bSSFP contrast produced predominantly T2-weighted images, but when necessary, a 90° saturation RF pulse was applied to obtain a predominant T1-weighting, which decreased the update rate to 475 ms.

A total of 20 RF electrodes were placed under MR fluoroscopy (Table 2). For 12 lesions, a single bipolar electrode was positioned at the centre of the tumour. Two electrodes were placed at the periphery of the target tumour when its long-axis diameter exceeded 2 cm ($n=2$) or when lying in contact with a large hepatic vessel ($n=2$) [19]. The final position of the RF electrodes with regard to the index tumour was verified on the 3D T1-weighted VIBE sequence. The distance between the target position and the centre of the active tip of the RF electrode was calculated according to their xyz coordinates with an open-source DICOM viewer (The OsiriX Foundation, Geneva, Switzerland) [20]. The duration of targeting was defined from the initial insertion of each electrode and confirmation of an acceptable position within the tumour.

RF ablation with temperature monitoring

RF energy application was done with settings as indicated by the manufacturer and in the same way as we usually

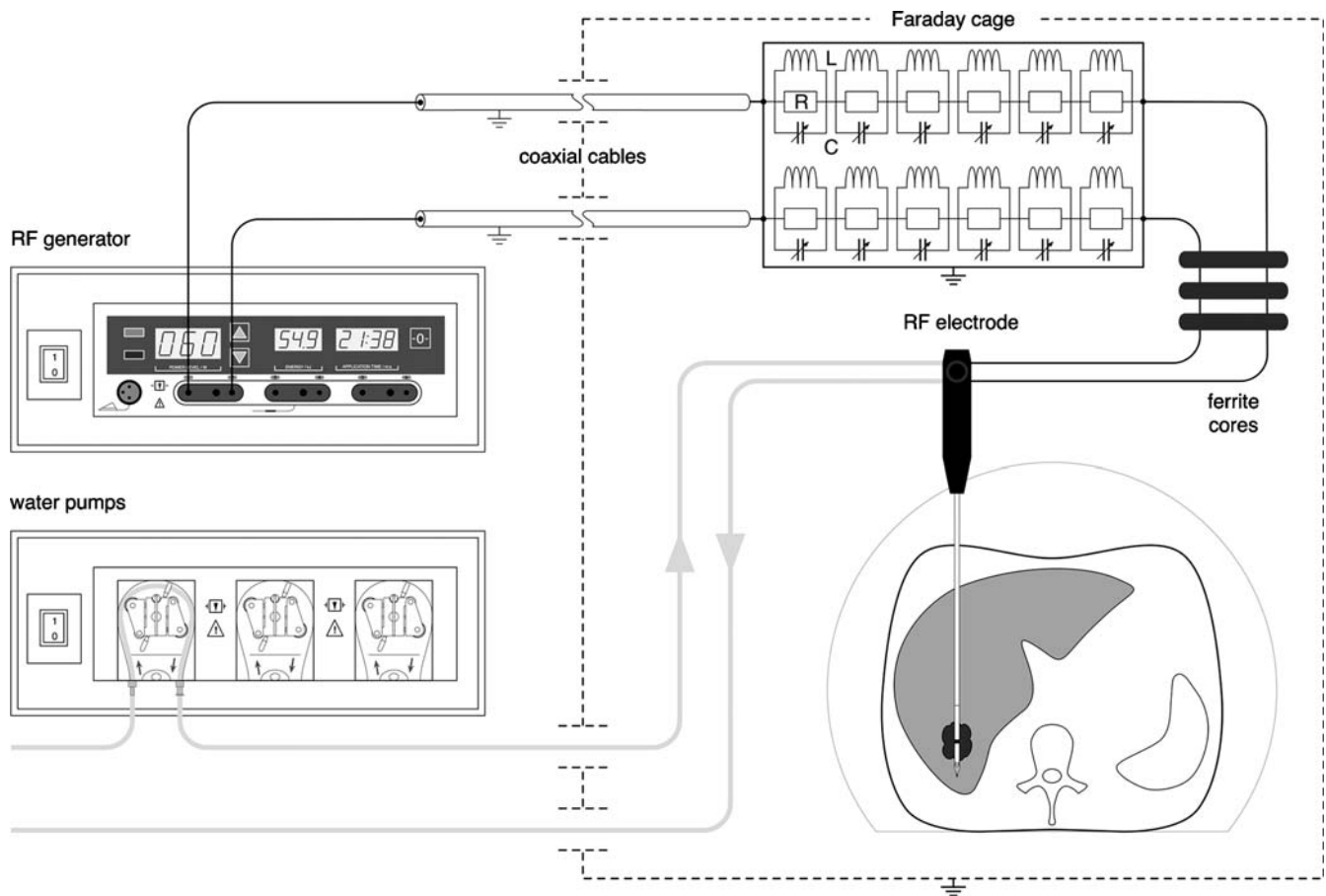


Fig. 1 Schematic of MR-compatible RF ablation setup. A commercial RF generator is placed outside the Faraday cage (FC). Coaxial cables connect the RF generator inside the FC with BNC (Bayonet Neill Concelman) connectors placed on a dedicated panel outside the FC. Inside the FC, the AC signal is filtered using, for each of the two lines, six stop-band passive parallel filter cells composed of resistors (R), inductors (L) and variable capacitors (C). The shield of the coaxial cables and the filter is connected to the

same potential as the FC. The cable between the filter box and the RF electrode is further filtered using three ferrite cores. The plastic tubes of the water circuit for internal cooling of the electrode go in and out through two waveguides of the FC. The generator was connected to the RF electrode after final positioning of the RF electrode. RF power is then applied simultaneously with the MR thermometry imaging

perform RF ablation under US or CT guidance. The physical parameters for each lesion were monitored on the first screen of an external PC (Table 2). At the end of RF application, electrode track coagulation was systematically performed.

MR thermometry was performed simultaneously during RF ablation, using the proton resonance frequency shift (PRFS) method and a lipid-suppressed segmented gradient echo–echo planar imaging (GRE-EPI) hybrid sequence, as already described and validated [21]. Three parallel slices were acquired in a single plane during the expiratory phase by means of pressure-sensor triggering, with the central slice positioned along the RF electrodes. Image parameters included: echo train length (ETL), 13; TR, 50 ms; TE, 20 ms; FA, 25°; BW, 1,000 Hz/pixel; matrix, 128×128; voxel size, 2.3×2.3×6.0 mm³; slice gap, 1.2 mm. The acquisition time was 0.6 s per slice and the sampling rate was equal to the respiratory frequency.

The magnitude and phase images were transferred on-line to the external PC for post-processing. The relative temperature measurements were derived from the time series of phase images and continuously processed with dedicated C⁺⁺ software (Image Guided Therapy, Pessac, France). A nasopharyngeal transducer monitored body temperature. The lethal thermal dose was calculated according to the empirical model of Sapareto [8, 22]. During RF application, the absolute isotherms and lethal thermal dose were displayed in real time on the second screen of the external PC (Table 3).

The SNR of the magnitude images and the temperature standard deviation (SD) in a non-heated region of interest (ROI) were calculated for each image in the dynamic series to characterize the efficiency of the RF device filtering and the temperature accuracy, respectively. Two radiologists qualitatively assessed the image quality of the isotherms and thermal dose maps.

Table 2 Physical parameters during RF ablation

Patient	Session number	Lesion number	Number of RF electrodes	Output power (W)	Effective power (W)	Total duration (min)	Total energy (kJ)
A	I	1	2 ^a	60/40	22.5	32.8	30.8
B	II	2	2	60	35.9	23.2	50.1
		3	2	60	40.9	15.0	36.1
		4	1	30	17.3	18.6	15.0
C	IV	5	2 ^a	60/20	32.5	46.4	75.9
	V	6	1 ^a	30/25	20.2	18.4	20.2
D	VI	7	1	50	36.8	18.1	40.0
		8	1 ^b	30	19.5	14.2	19.8
E	VII	9	1	30	17.7	15.8	16.7
F	VIII	10	1	30	13.3	33.2	26.5
		11	1	30	16.9	19.3	19.5
G	IX	12	1 ^a	30/20	19.9	36.7	36.2
H	X	13	1	30	19.1	22.0	25.3
I	XI	14	1	30	18.5	19.5	22.1
J	XII	15 ^c	1	30	19.7	18.0	24.3
		16 ^c	1	30	17.4	16.2	19.3

Effective power is the mean power during the whole procedure. A mean output power of 36.6 ± 11.7 W (20.0–60.0 W), with a corresponding mean effective power of 23.0 ± 8.4 W (13.3–40.9 W), was applied during 22.9 ± 9.3 min (14.2–46.4 min) for a total energy deposition of 29.9 ± 15.6 kJ (15.0–75.9 kJ)

^aRF electrode repositioning

^bRF electrode retraction

Controlling

At the end of RF application, electrode track coagulation was systematically performed. Post-ablation imaging protocol included the same T2-weighted HASTE and TSE sequences as used for the initial planning. Complete ablation was assumed when high T2 signal intensity was replaced by low signal intensity surrounded by a rim of high signal, encompassing the index tumour with an intended ablative margin of 5 mm. If remaining high signal intensity indicated residual tumour tissue, additional RF application was performed after repositioning of the electrodes.

The overall duration of the interventions from the admission to the exit of the patient from the MR suite was recorded according to the anaesthesia protocol.

Follow-up and clinical outcome

All patients stayed in the hospital overnight for medical observation and laboratory follow-up and were discharged after recovery. Twenty-four hours after RF procedure, a quadriphasic CT examination (section thickness, 2.0 mm; reconstruction interval, 1.0 mm) with intravenous contrast injection (Accupaque 350; GE Healthcare, Oslo, Norway; 2 mL/kg; rate, 3–5 mL/s) was performed for early complications.

Description of the results of RF ablation was based on international recommendations according to standard criteria [16, 23]. Follow-up consisted in MR imaging with hepato-specific contrast and monitoring of tumour markers at 1 week, 1 month and every 3 months. The primary technique effectiveness was assessed 1 month after a single RF session. Any hyperintensity on T2-weighted images or non-enhancing area on contrast-enhanced MR images at the boundaries of the treated area was considered as incomplete ablation. Local tumour progression was determined on subsequent follow-up imaging and the secondary technique effectiveness was evaluated in patients with 1-year or more follow-up.

Statistical analysis

Descriptive statistical values were presented as means, SD and ranges. Contrast-to-noise ratio (CNR) was calculated between liver and tumour, RF electrode or hepatic vessels: $CNR = |(SI_1 - SI_2)/SD_{noise}|$, where SI_1 is the signal intensity of the liver parenchyma, SI_2 is the signal intensity of the tumour, the RF electrodes or the hepatic vessels, and SD_{noise} is the SD of the background noise. Statistical analysis was performed with a commercially software (Prism version 5.0 for MacOSX; GraphPad Software, La Jolla, USA). Compar-

Table 3 Qualitative and quantitative parameters of temperature monitoring during RF ablation

Lesion number	Imaging plane	SNR	T°	SD	Image quality ^a	Lethal thermal dose during RF ablation		Ablation zone at 1-week MRI	
						Long-axis diameter (cm)	Short-axis diameter (cm)	Long-axis diameter (cm)	Short-axis diameter (cm)
1	Oblique coronal	16	N/A	Insufficient	–	–	–	4.2	2.3
2	Oblique sagittal	23	1.7	Insufficient	–	–	–	3.8	2.5
3	Oblique sagittal	34	0.8	Acceptable	3.9	2.6	4.4	2.4	2.4
4	Oblique axial	32	1.0	Acceptable	2.7	1.5	2.8	2.3	2.3
5	Oblique axial	26	1.4	Acceptable	5.9	4.5	3.3	3.1	3.1
6	Oblique sagittal	22	3.0	Acceptable	1.9	1.3	4.3	3.4	3.4
7	Oblique axial	26	0.7	Adequate	3.2	2.4	3.3	2.4	2.4
8	Oblique axial	37	2.0	Adequate	2.4	1.8	3.3	2.3	2.3
9	Oblique axial	11	3.5	Acceptable	3.1	2.1	4.2	2.2	2.2
10	Oblique sagittal	34	2.0	Acceptable	2.8	1.6	2.7	1.9	1.9
11	Oblique axial	40	1.7	Adequate	3.2	1.9	3.8	1.7	1.7
12	Oblique sagittal	22	1.6	Insufficient	–	–	3.7	2.6	2.6
13	Oblique axial	38	1.2	Adequate	2.7	1.7	3.2	2.2	2.2
14	Oblique axial	31	1.4	Acceptable	2.4	1.5	2.9	1.9	1.9
15	Oblique axial	26	0.8	Adequate	3.5	2.2	3.9	2.0	2.0
16	Oblique sagittal	16	N/A	Insufficient	–	–	3.6	1.9	1.9

The mean SNR was 27.1 ± 8.5 (11.0–40.0) and the temperature accuracy was $1.6 \pm 0.8^\circ\text{C}$ (0.7–3.5). The final thermal dose maps on the central slice were compared with the ablation zone on the MR imaging at 1 week, but Spearman analysis did not reveal any correlation between the long-axis diameters ($r=0.301$; $P=0.342$) and the short-axis diameters ($r=0.219$; $P=0.494$), respectively. SNR signal-to-noise ratio of the magnitude images, calculated as the mean of signal in a non-heated region of interest (ROI) more than 5 cm away from the RF electrode, divided by the standard deviation (SD) of pixels in a background noise ROI of 100 pixels, for each image in the dynamic series; T° SD mean standard deviation of temperature in the same non-heated ROI; N/A not available.

^aCriteria for image quality: adequate, no significant noise and lethal thermal dose is quantifiable; acceptable, significant noise, but lethal thermal dose is still visible; insufficient, significant noise that degrades the image to a great extent and the thermal maps are barely visible.

isons of the CNR measurements were performed with Mann–Withney *U* test. The duration of targeting on consecutive RF ablations was assessed with non-linear regression analysis. Spearman correlation coefficient was calculated to compare the size of lethal thermal dose with the ablation zone on imaging follow-up in the same imaging plane.

Results

Radiofrequency ablation procedures

The 12 RF sessions were completed under MR guidance in all cases. The overall duration of the interventions was 194 ± 33 min (141–256). At the end of each intervention,

complete tumour coverage by the ablation zone was obtained for the 16 malignant nodules, as assessed on T2-weighted images, for a technical success rate of 100%.

Planning

The conspicuity of seven lesions, which were not sufficiently visible on the unenhanced T1-weighted VIBE sequence ($CNR = 14 \pm 9$), was improved by the infusion of mangafodipir ($CNR = 33 \pm 20$). The T2-weighted HASTE ($CNR = 22 \pm 14$) and TSE with fat saturation ($CNR = 38 \pm 17$) sequences were useful to distinguish

local tumour progression from a previous ablation zone ($n=2$) or changes at the site of resection ($n=3$).

The RF electrode trajectory was easily planned with MPR techniques on the 3D T1-weighted VIBE acquisition and measured 10.9 ± 3.5 cm (6.0–15.5).

Targeting

The MR-compatible components of the in-room user interface did not interfere with sterility requirements, anaesthesia monitoring or placement of the RF electrode. The only drawback was that the operator's position needed

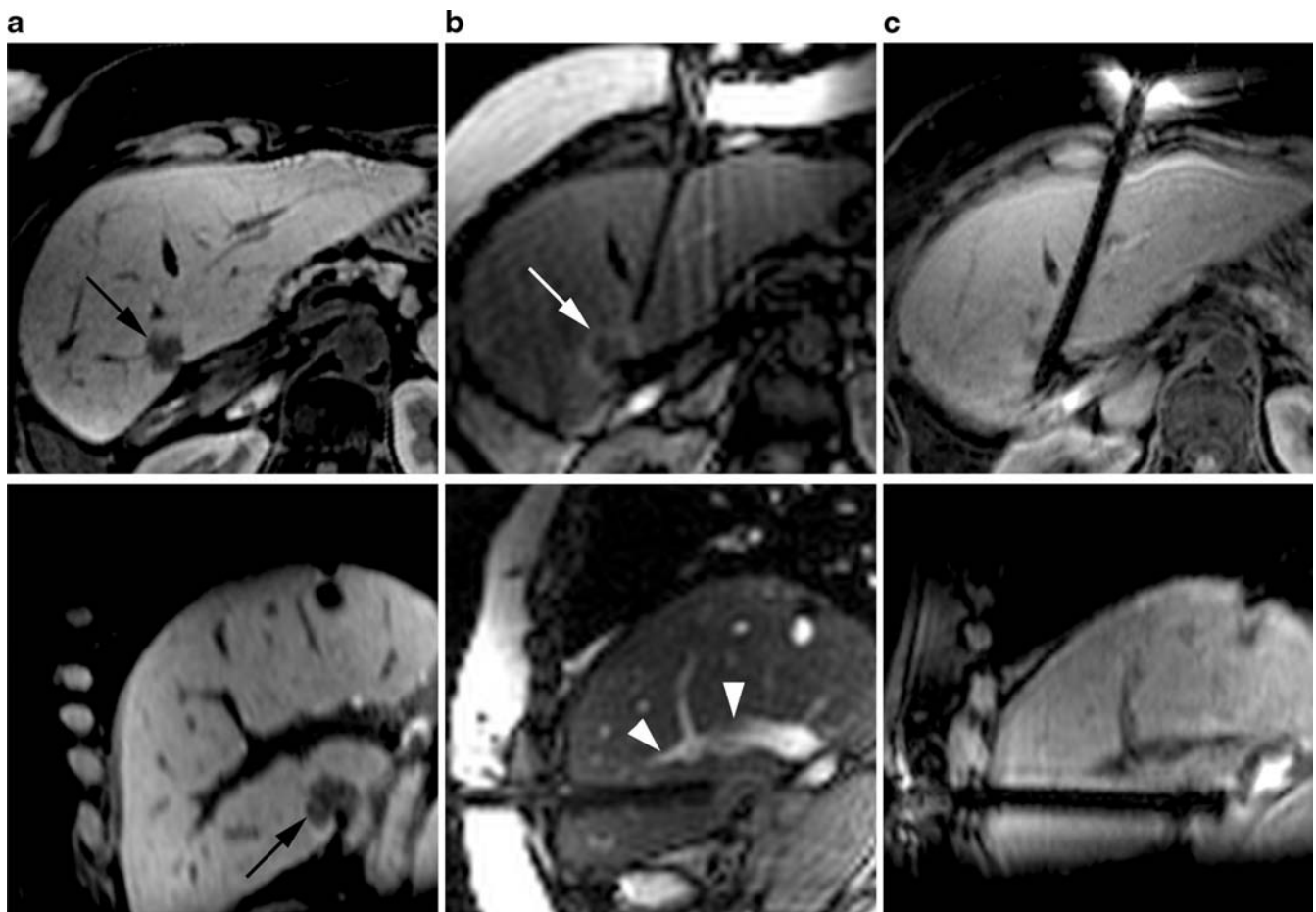


Fig. 2 Targeting under MR imaging of a recurrent nodule (lesion 4) in a 54-year-old woman (patient B) after right hepatectomy with four wedge resections for synchronous liver metastases of colorectal origin. **a** 3D T1-weighted VIBE images (TR, 5.6 ms; TE, 2.7 ms; FA, 10°; matrix, 320×256 ; section thickness, 2 mm) reconstructed in the axial oblique plane (top) and sagittal oblique plane (bottom) are used for planning. A 1.8-cm large, irregular and hypointense nodule (black arrows) at the posterior and inferior aspect of segment 4 and in contact with the site of a previous metastasectomy. **b** "Fluoroscopic" bSSFP sequence (TR, 4.3 ms; TE, 2.2 ms; FA, 70°; matrix, 128×128 ; section thickness 5 mm) shows the RF electrode

9 min and 14 s after its insertion at the entry site. The predominantly T1-weighted image (update rate, 475 ms) in the axial oblique plane (top) shows the proximity of the electrode tip with regard to the metastatic nodule (white arrow), whereas the predominantly T2-weighted image (update rate, 275 ms) in the sagittal oblique plane (bottom) demonstrates its relation with the left branch of the portal vein (white arrowheads). **c** At the end of the targeting procedure, a new 3D T1-weighted VIBE acquisition shows the final position of the active tip of the RF electrode within the tumour nodule in both orthogonal oblique planes

to be adapted to the magnet's bore during the initial targeting procedure.

Both T1- and T2-weighted variants of the bSSFP imaging sequence were useful in the targeting procedure (Fig. 2). The CNR measurements showed better tumour conspicuity on the T1-weighted images, whereas the vascular structures were better visualized on the T2-weighted images (Fig. 3). The width of the susceptibility artefact of the RF electrode was 0.6 ± 0.2 cm and 0.8 ± 0.3 cm on the T1- and T2-weighted images, respectively, without statistically significant difference between the oblique axial and sagittal planes.

During the 20 electrode placements, correct targeting was achieved with a precision of 0.4 ± 0.2 cm (0.1–0.8) and the duration of targeting was 21 ± 11 min (8–48). A typical learning curve was observed, which showed an initial reduction of targeting time to reach a plateau on subsequent procedures (Fig. 4). Conversely, no correlation was observed between the distance of the tumour from the skin surface and the duration of targeting.

RF ablation with temperature monitoring

Hardware filtering provided a mean attenuation of -95 ± 5 dB at 63.5 MHz. The same SNR in magnitude images was obtained with the generator in standby mode or power application mode, regardless of the actual power level and duration for a specific procedure ($P=0.768$).

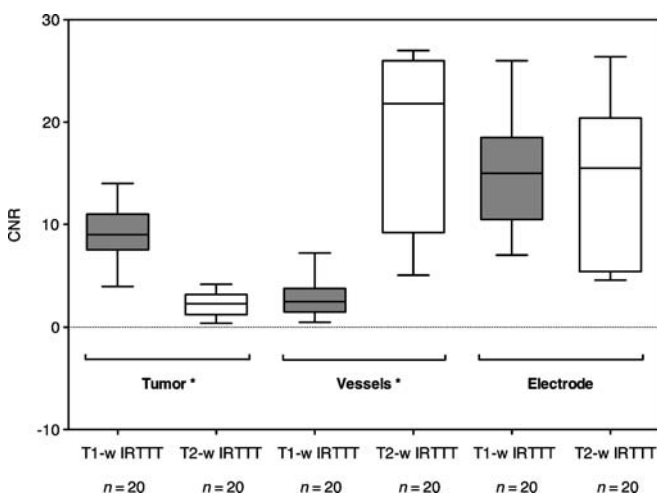


Fig. 3 Graph shows the CNR of T1-weighted bSSFP images (T1-w IRTTT in grey) and T2-weighted bSSFP images (T2-w IRTTT in white) in three situations: CNR of the tumour target, the hepatic vessels or the RF electrode with regard to liver parenchyma. Boxes represent the interquartile range, which contains 50% of values. Lines across the boxes indicate the median, whereas error bars indicate maximum and minimum values. Asterisks specify a statistically significant difference between two unpaired groups for tumour ($P=0.0001$) and vessels ($P=0.0003$), but not for the RF electrode ($P=0.871$)

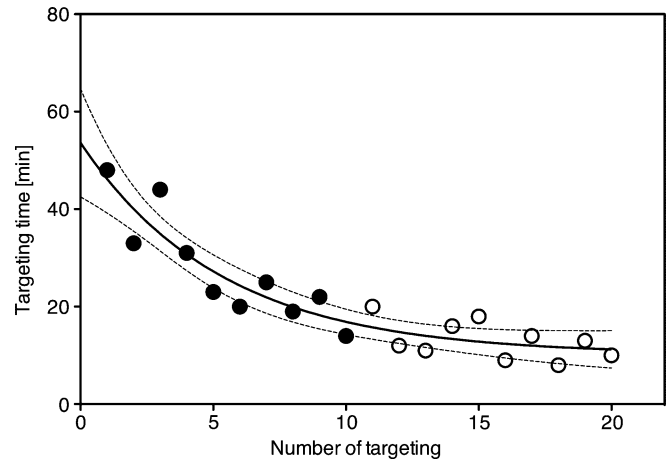


Fig. 4 The targeting learning curve. The duration of targeting was 28 ± 11 min for the initial procedures (black circles; $n=10$) and 13 ± 4 min for the following ones (white circles; $n=10$) with a statistically significant difference ($P=0.0008$) between these two groups. The values are correctly fitted by ($R^2=0.869$) one-phase decay exponential regression (solid curve) within a 95% confidence interval (dashed curves)

MR thermometry was achievable during RF ablation in 14 of the 16 treated nodules (88%) with a mean SD of 1.6°C in a non-heated ROI (Fig. 5). The final lethal thermal dose was assessable in 12 of the 16 RF applications (75%).

The width of the susceptibility artefact of the RF electrode was 1.2 ± 0.3 cm, without statistically significant difference over the series of treatments regardless of the imaging plane. Image quality for the GRE-EPI sequence was better when acquisition was performed in the oblique axial than in the oblique sagittal or coronal plane. The cause of insufficient image quality was mainly related to problems of respiratory triggering, when general anaesthesia was suboptimal and the patient presented involuntary diaphragm contraction.

No statistically significant correlation was found between the size of the lethal thermal dose and the ablation zone at 24-h CT, 1-week, 1-month or 3-month MR imaging. In four nodules close to a large hepatic vessel, the thermal dose maps revealed local asymmetry with a thinning or a notch at the side of the vessel (Fig. 6).

Controlling

At the end of RF application, four ablation zones showed residual hyperintensity on T2-weighted images at their boundaries that were interpreted as incomplete ablation. After repositioning of the electrode, a second ablation was performed in order to obtain complete tumour coverage. The second procedure resulted in signal loss in all instances.

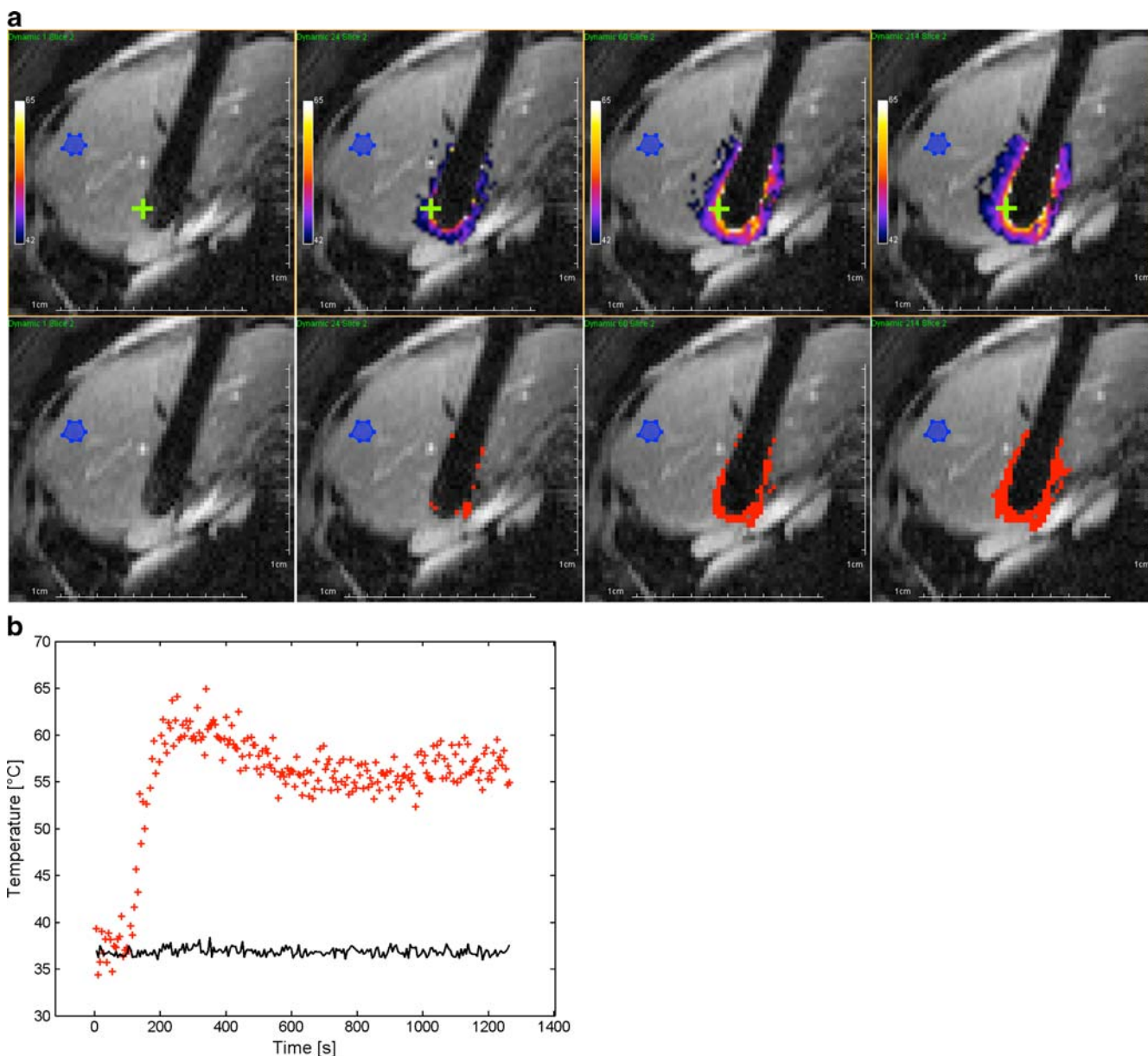


Fig. 5 RF ablation with real-time monitoring of the same nodule shown in Fig. 2. **a** The successive isotherms (top) and thermal dose (bottom) images on the central slice of GRE-EPI sequence (ETL, 13; TR, 50 ms; TE, 20 ms; FA, 25°; matrix, 128×128; section thickness, 6 mm; plane, axial) show the time evolution (left to right: $t=5.5$ s; $t=132$ s; $t=330$ s; $t=1,175$ s) of isotherms and thermal dose maps, respectively. Colour range is set from 42 to 65°C (top) and regions above one lethal threshold of cumulative thermal dose (bottom), corresponding to 240 equivalent minutes at 43°C, are shown in red.

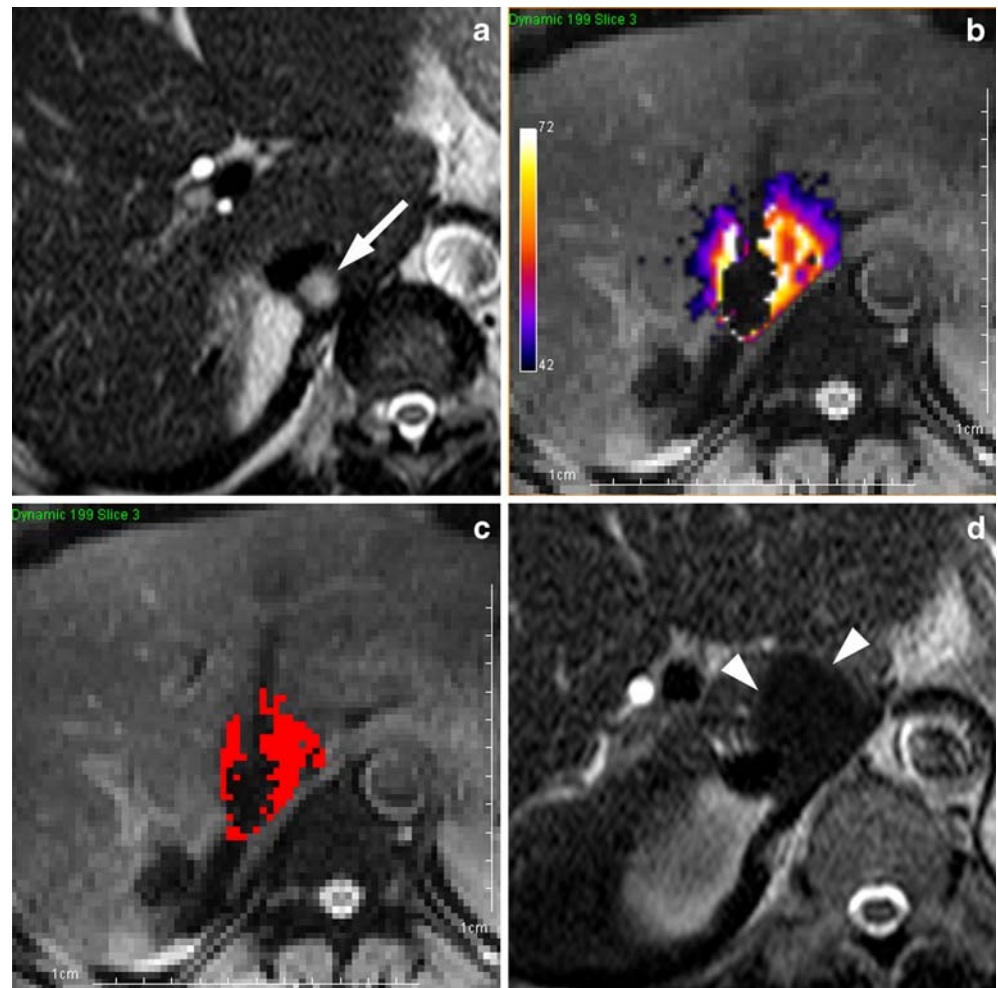
The width of susceptibility artefact of the RF electrode is 1.8 cm. **b** Temperature evolution during the RF ablation on the same timescale. A non-heated ROI was selected (blue ROI in Fig. 5a) to monitor the standard deviation of temperature (SD=1.0°C) (solid black line). One pixel was selected on the thermal maps (green cross in Fig. 5a) to illustrate the temperature time evolution (red crosses). Three phases are observed: the baseline, the rapid increase and the stabilization of temperature. The uncertainty of temperature in the heated region is higher than in the non-heated region

Follow-up and clinical outcome

The mean duration of hospitalisation was 2.3 ± 0.7 days (1.1–3.7). There were no major complications related to the ablation procedure. One minor complication (8.3%) occurred among the 12 RF sessions and consisted in a

first-degree skin burn at the puncture site. This was related to track ablation and resolved completely after topical application of diclofenac cream and oral intake of ibuprofen. Post-ablation syndrome occurred after two RF sessions (17%), but was self-limited and did not significantly lengthen the hospital stay.

Fig. 6 Monitoring and controlling of RF ablation in a 57-year-old man (patient D) with a metastatic nodule from colorectal cancer (lesion 7) in segment 1, which was already treated by RF ablation under US guidance. **a** Axial HASTE T2-weighted image (TR, 1,000 ms; TE, 83 ms; FA, 150°; matrix size, 256×224; section thickness, 4 mm) shows a 1.3-cm large nodule (*white arrow*) with hyperintense signal, corresponding to local tumour progression within the ablation zone in close contact with the inferior vena cava (IVC). **b,c** Temperature (*b*) and thermal dose (*c*) maps on the central slice of GRE-EPI sequence (ETL, 13; TR, 50 ms; TE, 20 ms; FA, 25°; matrix, 128×128; section thickness, 6 mm; plane, axial) at the end of RF ablation (1,094.5 s or 199 dynamics) show frank asymmetry in shape, because the RF electrode is placed between the tumour nodule and the IVC, which results in an important heat sink effect. **d** Axial HASTE T2-weighted image at immediate control after RF ablation shows the typical signal drop within the ablation zone (*white arrowheads*). At 15-month follow-up, no local tumour progression was detected by MR imaging (*not shown*) and the IVC was still patent



The mean follow-up period was 19 ± 7 months (3–26). At 1-month MR imaging, complete tumour destruction was achieved after one RF session in all 16 malignancies, for a primary effectiveness rate of 100%. On subsequent follow-up, local tumour progression was observed in two patients at 3 and 10 months. In patient C, the local tumour progression was successfully re-treated under MR guidance. Secondary technique effectiveness was observed in 10 of the 11 tumours (91%) with 1-year or more follow-up. New hepatic and extra-hepatic tumours appeared in two patients with metastases from colorectal cancer and in the patient with metastases from lung carcinoma. No tumour seeding was observed during follow-up. One patient with colorectal cancer died from disseminated disease 17 months after RF ablation.

Discussion

The present study shows that RF ablation of small liver tumours can be done entirely and effectively with MR guidance. It is well known that some small liver neoplasms

cannot be well visualised with contrast-enhanced US or CT. Such nodules may still be amenable to image-guided treatment by combining different techniques, such as CT–US fusion imaging-guided RF ablation, intraoperative RF ablation or combined TACE and RF ablation for HCC. However, none of our ten patients could have been treated with RF ablation alone without using our technique. From a practical point of view, MR-guided electrode placement has generally been a lengthy procedure, thus occupying precious machine time that is usually for diagnostic imaging and hampering the development of MR imaging for interventional purposes in many institutions. The dedicated interventional MR system used in this study enabled us to overcome this drawback by significantly reducing the time for targeting.

The hardware components adapted to the MR environment proved suitable for the interventional procedure. The 70-cm-diameter bore of the magnet, as well as the flexible coil, provided adequate space and distances for intervention under antiseptic conditions. The “interventional” bSSFP sequence provided sufficient CNR for the targeting of most lesions, and when adding the T1-weighted images

with hepato-specific contrast materials, all lesions could be targeted adequately. Furthermore, the high temporal resolution of the bSSFP sequence with the multiplanar capabilities of the GSP software rendered the MR-guided procedure faster than with previously reported MR-based techniques [11–13]. In a recent study, the authors reported similar findings for MR-guided RF ablation of renal cell carcinoma in two patients [14]. With increasing practical experience, it should be possible to further reduce the procedure duration.

The concept of thermal dose mapping is currently the only semi-quantitative criteria used to predict heat-induced tissue damage [22]. So far, few papers have reported studies of in vivo MR thermometry under RF heating. Two animal studies compared thermal dose and the final ablation zone, but showed controversial results [24, 25]; and one case report described the use temperature monitoring during RF ablation in a cirrhotic patient [15]. Ideally, it is desirable to define a patient-specific endpoint for RF energy deposition based on real-time MR thermometry data. By using the current filtering technique, temperature and thermal dose maps can be obtained simultaneously during RF application in most cases. This is in contrast with the previously reported technique of switching between power application and imaging, which significantly lengthens the procedure [26]. Nonetheless, the clinical usefulness of thermal dose mapping remains questionable and the T2-based signal changes after application of an empirically determined dose of energy appears to be a more reliable indicator for the endpoint of RF ablation [27, 28].

The PRFS-based MR-thermometry should be more systematically accurate to assess for the validity of empirical thermal dose model, whereas correlation studies with a larger number of patients are needed in the future. Further technical refinements should focus on the RF

electrode's alloy formulation in order to minimise the susceptibility artefact on MR images, which may cancel the temperature signal exactly where it should have been measured. Another issue to be addressed is the robustness of the GRE-EPI temperature images toward liver respiratory motion, since through-plane motion may affect the accuracy of thermometry. More sophisticated techniques, such as multi-reference or reference-less methods, may lead to improvements in the future [29, 30]. Even though the actual software acquires only three parallel slices in a single plane, it seems that image quality is also dependent on the imaging plane orientation. Further development should include MR monitoring of temperature variations in three orthogonal slices, a first step toward 3D thermometry.

In conclusion, our preliminary clinical experience suggests that all steps of RF ablation, namely planning, targeting, monitoring and controlling, are technically feasible with MR imaging. The interactive targeting mode enables effective and sufficiently rapid electrode placement in clinical practice. Additional clinical experience is needed to determine if thermal dose mapping can be used to determine the endpoint of RF ablation. Such future improvements could help to render RF ablation of liver tumours more precise and reproducible, especially when the nodule is close to a large vessel and the perfusion-mediated tissue cooling affects the evolution of the ablation zone.

Acknowledgments The authors would like to thank André Roggan, PhD (Celon AG), Jörg Roland, PhD (Siemens Medical Solutions) and Erik Dumont, PhD (Image Guided Therapy) for valuable assistance and technical support.

This work was supported by the Swiss National Science Foundation–National Center for Competence in Research (NCCR), Computer-Aided Medical Interventions (CO-ME) Phase 2 Funding n° 51NF40–111383.

References

1. Llovet J, Bruix J (2008) Novel advancements in the management of hepatocellular carcinoma in 2008. *J Hepatol* 48(Suppl 1):20–37. doi:10.1016/j.jhep.2008.01.022
2. Lencioni R, Crocetti L (2008) Image-guided thermal ablation of hepatocellular carcinoma. *Crit Rev Oncol Hematol* 66:200–207. doi:10.1016/j.critrevonc.2008.01.003
3. Mentha G, Majno P, Terraz S et al (2007) Treatment strategies for the management of advanced colorectal liver metastases detected synchronously with the primary tumour. *Eur J Surg Oncol* 33(Suppl 1):76–83. doi:10.1016/j.ejso.2007.09.016
4. Reuter NP, Woodall CE, Scoggins CR, McMasters KM, Martin RC (2009) Radiofrequency ablation vs resection for hepatic colorectal metastasis: therapeutically equivalent. *J Gastrointest Surg* 13:486–491. doi:10.1007/s11605-008-0727-0
5. Willatt JM, Hussain HK, Adusumilli S, Marrero JA (2008) MR Imaging of hepatocellular carcinoma in the cirrhotic liver: challenges and controversies. *Radiology* 247:311–330. doi:10.1148/radiol.247061331
6. Onishi H, Murakami T, Kim T et al (2006) Hepatic metastases: detection with multi-detector row CT, SPIO-enhanced MR imaging, and both techniques combined. *Radiology* 239:131–138. doi:10.1148/radiol.2383041825
7. Bipat S, van Leeuwen M, Comans E et al (2005) Colorectal liver metastases: CT, MR imaging, and PET for diagnosis—meta-analysis. *Radiology* 237:123–131. doi:10.1148/radiol.2371042060
8. Quesson B, de Zwart JA, Moonen CT (2000) Magnetic resonance temperature imaging for guidance of thermotherapy. *J Magn Reson Imaging* 12:525–533
9. Cernicanu A, Lepetit-Coiffé M, Viallon M, Terraz S, Becker CD (2007) New horizons in MR-controlled and monitored radiofrequency ablation of liver tumours. *Cancer imaging* 7:160–166. doi:10.1102/1470-7330.2007.0022

10. de Senneville B, Mougenot C, Quesson B, Dragonu I, Grenier N, Moonen C (2007) MR thermometry for monitoring tumor ablation. *Eur Radiol* 17:2401–2410. doi:[10.1007/s00330-007-0646-6](https://doi.org/10.1007/s00330-007-0646-6)
11. Kelekis A, Terraz S, Roggan A et al (2003) Percutaneous treatment of liver tumors with an adapted probe for cooled-tip, impedance-controlled radiofrequency ablation under open-magnet MR guidance: initial results. *Eur Radiol* 13:1100–1105. doi:[10.1007/s00330-003-1847-2](https://doi.org/10.1007/s00330-003-1847-2)
12. Clasen S, Pereira P (2008) Magnetic resonance guidance for radiofrequency ablation of liver tumors. *J Magn Reson Imaging* 27:421–433. doi:[10.1002/jmri.21264](https://doi.org/10.1002/jmri.21264)
13. Clasen S, Boss A, Schmidt D et al (2007) MR-guided radiofrequency ablation in a 0.2-T open MR system: technical success and technique effectiveness in 100 liver tumors. *J Magn Reson Imaging* 26:1043–1052. doi:[10.1002/jmri.21120](https://doi.org/10.1002/jmri.21120)
14. Boss A, Rempp H, Martirosian P et al (2008) Wide-bore 1.5 Tesla MR imagers for guidance and monitoring of radiofrequency ablation of renal cell carcinoma: initial experience on feasibility. *Eur Radiol* 18:1449–1455. doi:[10.1007/s00330-008-0894-0](https://doi.org/10.1007/s00330-008-0894-0)
15. Laumonier H, Blanc JF, Quesson B et al (2006) Real-time monitoring of hepatocellular carcinoma radiofrequency ablation by quantitative temperature MRI. *Semin Liver Dis* 26:391–397. doi:[10.1055/s-2006-951605](https://doi.org/10.1055/s-2006-951605)
16. Goldberg SN, Grassi CJ, Cardella JF et al (2005) Image-guided tumor ablation: standardization of terminology and reporting criteria. *Radiology* 235:728–739. doi:[10.1148/radiol.2353042205](https://doi.org/10.1148/radiol.2353042205)
17. Bruix J, Sherman M (2005) Management of hepatocellular carcinoma. *Hepatology* 42:1208–1236. doi:[10.1002/hep.20933](https://doi.org/10.1002/hep.20933)
18. Frericks BB, Ritz JP, Roggan A, Wolf KJ, Albrecht T (2005) Multipolar radiofrequency ablation of hepatic tumors: initial experience. *Radiology* 237:1056–1062. doi:[10.1148/radiol.2373041104](https://doi.org/10.1148/radiol.2373041104)
19. Terraz S, Constantin C, Majno PE, Spahr L, Mentha G, Becker CD (2007) Image-guided multipolar radiofrequency ablation of liver tumours: initial clinical results. *Eur Radiol* 17:2253–2261. doi:[10.1007/s00330-007-0626-x](https://doi.org/10.1007/s00330-007-0626-x)
20. Rosset A, Spadola L, Pysher L, Ratib O (2006) Informatics in radiology (infoRAD): navigating the fifth dimension: innovative interface for multi-dimensional multimodality image navigation. *Radiographics* 26:299–308. doi:[10.1148/rg.261055066](https://doi.org/10.1148/rg.261055066)
21. Cernicanu A, Lepetit-Coiffe M, Roland J, Becker CD, Terraz S (2008) Validation of fast MR thermometry at 1.5 T with gradient-echo echo planar imaging sequences: phantom and clinical feasibility studies. *NMR Biomed* 21:849–858. doi:[10.1002/nbm.1267](https://doi.org/10.1002/nbm.1267)
22. Sapareto SA, Dewey WC (1984) Thermal dose determination in cancer therapy. *Int J Radiat Oncol Biol Phys* 10:787–800
23. Leoni CJ, Potter JE, Rosen MP, Brophy DP, Lang EV (2001) Classifying complications of interventional procedures: a survey of practicing radiologists. *J Vasc Interv Radiol* 12:55–59
24. Vigen K, Jarrard J, Rieke V, Frisoli J, Daniel B, Butts Pauly K (2006) In vivo porcine liver radiofrequency ablation with simultaneous MR temperature imaging. *J Magn Reson Imaging* 23:578–584. doi:[10.1002/jmri.20528](https://doi.org/10.1002/jmri.20528)
25. Lepetit-Coiffé M, Quesson B, Seror O et al (2006) Real-time monitoring of radiofrequency ablation of rabbit liver by respiratory-gated quantitative temperature MRI. *J Magn Reson Imaging* 24:152–159. doi:[10.1002/jmri.20605](https://doi.org/10.1002/jmri.20605)
26. Zhang Q, Chung YC, Lewin JS, Duerk JL (1998) A method for simultaneous RF ablation and MRI. *J Magn Reson Imaging* 8:110–114. doi:[10.1002/jmri.1880080122](https://doi.org/10.1002/jmri.1880080122)
27. Mertyna P, Dewhirst MW, Halpern E, Goldberg W, Goldberg SN (2008) Radiofrequency ablation: the effect of distance and baseline temperature on thermal dose required for coagulation. *Int J Hypertherm* 4:1–10. doi:[10.1080/02656730802035662](https://doi.org/10.1080/02656730802035662)
28. Dromain C, de Baere T, Elias D et al (2002) Hepatic tumors treated with percutaneous radio-frequency ablation: CT and MR imaging follow-up. *Radiology* 223:255–262. doi:[10.1148/radiol.2231010780](https://doi.org/10.1148/radiol.2231010780)
29. Vigen KK, Daniel BL, Pauly JM, Butts K (2003) Triggered, navigated, multi-baseline method for proton resonance frequency temperature mapping with respiratory motion. *Magn Reson Med* 50:1003–1010. doi:[10.1002/mrm.10608](https://doi.org/10.1002/mrm.10608)
30. Rieke V, Vigen KK, Sommer G, Daniel BL, Pauly JM, Butts K (2004) Referenceless PRF shift thermometry. *Magn Reson Med* 51:1223–1231. doi:[10.1002/mrm.20090](https://doi.org/10.1002/mrm.20090)